applied sciences

MDPI

Article

Optimizing $CuFeS_2$ Chalcopyrite Thin Film Synthesis: A Comprehensive Three-Step Approach Using Ball-Milling, Thermal Evaporation, and Sulfurization Applied for Thermoelectric Generation

Marcelo Augusto Malagutti, Ketan Lohani, Mirco D'Incau, Himanshu Nautiyal, Narges Ataollahi and Paolo Scardi *

Department of Civil, Environmental and Mechanical Engineering, University of Trento, Via Mesiano 77, 38123 Trento, Italy; marcelo.malagutti@unitn.it (M.A.M.); ketan.lohani@unitn.it (K.L.); himanshu.nautiyal@unitn.it (H.N.); narges.ataollahi@unitn.it (N.A.)
* Correspondence: paolo.scardi@unitn.it

Abstract: $CuFeS_2$ (CFS) stands out as a promising narrow band-gap semiconductor for thermoelectric (TE) applications. However, its high lattice thermal conductivity is one of the factors hampering its potential for TE generation. A common strategy for tackling this problem is to produce this material in thin film form. Thus, this study aims to practically understand and optimize the synthesis of CFS 2D materials using a simple three-step approach of ball-milling, thermal evaporation, and sulfurization of the CuFe metallic precursors. The tools for thin film characterization employ X-ray Diffraction (XRD), Scanning Electron Microscopy (SEM), Energy-Dispersive X-ray Spectroscopy (EDXS), and Hall-effect measurements. DFT phase diagrams are also used to understand the energy of formation of the secondary phases present in the film. Here, we highlight that the ball-milling mechanisms, allied with high vacuum and high energy density during evaporation, are essential for the interdiffusion of Cu and Fe during the evaporation process. The film presented a flower-like morphology and *p*-type semiconducting behavior. A proof-of-concept Thermoelectric Generator (TEG) was designed in an in-plane geometry, showing a power output per unit active area of 114 nW cm^{-2} (ΔT = 180 °C), comparable to other Cu-based materials, thus demonstrating the feasibility of this method of synthesis for TE applications.

Keywords: $CuFeS_2$; thermal evaporation; thermoelectric generator; ball-milling; phase diagram

Citation: Malagutti, M.A.; Lohani, K.; D'Incau, M.; Nautiyal, H.; Ataollahi, N.; Scardi, P. Optimizing $CuFeS_2$ Chalcopyrite Thin Film Synthesis: A Comprehensive Three-Step Approach Using Ball-Milling, Thermal Evaporation, and Sulfurization Applied for Thermoelectric Generation. *Appl. Sci.* **2023**, *13*, 10172. https://doi.org/10.3390/app131810172

Academic Editor: José A. Jiménez

Received: 15 August 2023
Revised: 2 September 2023
Accepted: 7 September 2023
Published: 10 September 2023

1. Introduction

Chalcopyrites are a class of ternary materials with a diamond-like *I-42d* crystal structure. They present an opposite heat transport mechanism to the Keyes theory [1,2], meaning that its thermal conductivity increases with the lower mean atomic mass of the compound. The best-performing chalcopyrites for thermoelectric (TE) applications rely on the use of elemental Se, In, and Te [3,4]. However, they are considered either toxic or rare, leaving the sulfide-based chalcopyrites as a cheaper option for energy applications. Among them, $CuFeS_2$ (CFS) stands as one of the most abundant copper ore minerals [5], presenting a narrow band-gap (0.5 eV), high electrical conductivity (σ), and Seebeck (S) coefficient (~−480 μV/K) [6]. For CFS, its light constituent elements and Zn blend structure mean that the lattice thermal conductivity is large, thus resulting in poor TE performance in its bulk and undoped form [7]. Other Cu-Fe-S phases such as cubic bornite Cu_5FeS_4 (*Fm-3m*) [8,9], cubic $Cu_{18}Fe_{16}S_{32}$ talnakhite (*I-43m*) [10], and metastable hexagonal Wurtzite-type $CuFeS_2$ ($P6_3mc$) [11] do not suffer from this problem since they present significant disorder in their structure, stemming from their cation-vacancy mechanism. However, the chalcopyrite CFS phase persists as the most stable phase and is frequently employed for practical applications [12].

For bulk CFS materials, the reduction in the thermal conductivity (κ) relies on strategies such as nanostructuring [7,13], doping [14–17], the use of a sulfur-deficient stoichiometry [12], and/or a combination of them. Nanostructuring induces so-called phonon-glass electron-crystal behavior [18], where the grain boundaries of the crystallites scatter the phonon waves transporting heat without a significant decrease in σ. This strategy reduced CFS thermal conductivity by 47%, although the electron-crystal behavior was compromised [7]. Other than that, lattice engineering via doping and vacancy induction can promote more obstacles to phonon propagation within the lattice. Even though intrinsic doping can significantly enhance the power factor of CFS due to the introduction of more charge carriers into the system, the drop of lattice κ is still not satisfactory. According to T. Mori et al. [7], the reason is that the phonon waves responsible for heat transportation have a wavelength of about 100–1000 nm. To block the propagation of these phonons, they suggest transforming the material into a thin film form, having a thickness around the value of the phonon wavelengths.

Practical ways to employ thin film materials as Thermoelectric Generators (TEGs) employ an in-plane π geometry [19,20]. For these TEGs, *p*- and/or *n*-type legs are deposited in a flat substrate, displaced electrically in series and thermally in parallel, conveniently joined by metallic contacts. Upon heating one of its extremities, electrical energy is produced. To the best of our knowledge, no CFS in-plane generator has been fabricated in this manner. Nonetheless, various techniques are employed to convert bulk CFS into thin films. They include sputtering [11] from high-density spark-plasma sintered (SPS) materials [7,12,21], flash methods [22,23], spray pyrolysis [24–26], and thermal evaporation [27]. Evaporation is considered the cheapest and least complex method due to its higher deposition rate and the use of readily available powders. However, the different melting points of Cu and Fe mean that additional treatments are needed to promote the intermixing between the two. A strategy to solve this issue is proposed by Barkat et al. [27], where the targeted substrates are heated while multiple Cu/Fe layers are being deposited. The substrates are later exposed to a sulfur-rich atmosphere, a process called sulfurization, in order to introduce sulfur into the structure.

Thus, the current study introduces a novel three-step method for CFS fabrication using a previous ball-milling step prior to the thermal evaporation and sulfurization processes. The optimization of every synthesis process is thoroughly discussed, with the intention of providing a clear and instructive roadmap for future fabrication of this material in thermoelectricity (TE) and other potential fields. This optimization comprises tests on the evaporation of the non-milled powders (Section 3.1.1) and the milling parameters (Section 3.1.2). Characterization of the optimized film uncovers its structural properties, phase purity, surface morphology, and stoichiometry balance through X-ray Diffraction (XRD), Scanning Electron Microscopy (SEM), Electron Dispersive X-ray Spectroscopy (EDXS) analysis, and Hall-effect measurements (Section 3.2). To gain further insights into secondary phase formations within the phase diagram, Density Functional Theory (DFT) calculations are also employed. The viability of this synthesis approach is substantiated by the fabrication of a proof-of-concept Thermoelectric Generator (TEG), having its specific power output measured using I-V curves. In Section 4, we provide commentary and comparisons regarding this synthesis route, along with an exploration of potential applications.

2. Materials and Methods

2.1. Ball-Milling of the Metal Precursors

The elemental powders of Cu (−100~+325 mesh, 99.9%, Alfa Aesar) and Fe (−20 mesh, 99.9%, Alfa Aesar) were milled in three batches (namely, FeCu-01, $Fe_{1.76}$Cu-02, and FeCu-03) and their milling parameters are displayed in Table S1 of the Supplementary Note S1. The milling procedure employed a Fritsch P4 planetary ball mill equipped with WC vials (80 mL of volume) and 12 mm balls of the same material, keeping a Ball-to-Powder (BPR) ratio of 100:1. The rotation was set to 310 rpm for the main disk, with a −1.80 main disk-to-planet

ratio. Ethanol (99%, Sigma Aldrich, St. Louis, MO, USA) was used as a lubricant in the last batch, which helped with the retrieval of the as-milled powder from the vial and better microstructural homogenization.

2.2. Cu-Fe Thin-Film Deposition by Evaporation

The thin films were deposited on soda-lime glass (SLG) substrates using a thermal evaporator (Tecuum AG VCM600 V1) with a voltage of 12 V. The deposition parameters are displayed in Table S2 for Samples 1 to 18. Substrates were washed using a concentrated KOH solution and commercial soap, further rinsed with ultra-pure water, and dried using an air gun. For some samples, the SLG substrate was polished using sandpaper to improve adhesion.

2.3. Sulfurization Processes

The sulfurization parameters were carefully chosen through a process of iterative experimentation. It was carried out in a tubular furnace (Carbonite Gero, Sheffield, UK) at 500 °C (heating rate: 10 °C min^{-1}) and 425 °C (heating rate: 20 °C min^{-1}) for 1 h, using two different settings: (1) static Ar atmosphere and (2) dynamic N_2 flux, respectively. The Cu-Fe samples were placed in a carbon sample holder sided by a crucible containing 50 mg of S (−325 mesh, 99.5%, Alfa Aesar, Haverhill, MA, USA).

2.4. X-ray Diffraction

The XRD measurements were conducted in a Bruker (Billerica, MA, USA) D8 Discover diffractometer in θ-2θ configuration. The diffractometer was equipped with a Co Kα source (λ = 1.7889 Å) and 192 microstrip channels (1D configuration) detector. The illumination area was fixed to 1 × 8 mm^2. XRD data were collected from 2θ = 15° to 95°, with a step size of 0.05° and a collection time of 1 s per step. The phase identification was performed using ICSD [28] and PDF4+ [29] databases. Rietveld and line profile analysis were performed using the commercial version of TOPAS 6 (Bruker) software [30]. The instrumental profile was retrieved using a LaB_6 (NIST SRM 660c) standard sample [31]. A double-Voigt profile was employed for the microstructural analysis. One of the Voigt functions is attributed to crystallite size, where its integral breadth (β) is related to the mean volumetric crystallite size (Lvol) according to the Scherrer equation (see TOPAS manual for details [30]). The microstrain (ϵ) is obtained by the equation $\epsilon = \beta_{FWHM} \tan(\theta)$, where β_{FWHM} is the full width half maximum of the diffraction peak and θ is the diffraction angle. A March–Dollase approach was employed for the estimation of preferred orientation in the prepared films [30].

2.5. Scanning Electron Microscopy and Energy Dispersive X-ray Spectroscopy

SEM micrographs were collected with a JSM-7001F FEGSEM (JEOL, Tokyo, Japan) instrument equipped with an energy-dispersive X-ray spectroscopy detector (EDXS, Oxford INCA PentaFETx3, Oxford, UK). The electron beam energy was in the range of 10–15 keV, with a working distance of 5 to 10 mm. The morphology of the thin films was acquired in a top-down configuration and was later placed vertically in a stub to perform the cross-sectional analysis.

2.6. Computational Methods

The Vienna Ab initio Simulation Package (VASP) [32,33] as used to perform DFT calculations on the Cu-Fe-S system. The generalized gradient approximation with Perdew–Burke–Ernzerhof (PBE) [34] electron exchange-correlation was employed. The energy cut-off was set at 500 eV, and the structures were relaxed using the conjugate gradient algorithm until the force on each atom was less than 0.001 eV/Å. The electronic convergence was set to 10^{-6} eV. The specific k-point mesh employed for each system were as follows: $CuFeS_2$ (8 × 8 × 4), Cu_3Fe (8 × 6 × 8), Cu_7S4 (6 × 6 × 4), CuS (4 × 6 × 8), CuS_2 (4 × 6 × 8), Fe_3Cu (8 × 6 × 4), FeS (6 × 6 × 4), FeS_2 (6 × 6 × 4), bornite (4 × 4 × 4), and talnakhite (6 × 6 × 6).

Spin polarization was considered to account for the effects of electron spin interactions. The bornite and talnakhite structures were modeled using 160-atom and 64-atom cells, respectively, with the lattice parameters obtained from experiments in each case. Both compounds exhibited random occupation of Cu and Fe atoms, and pseudorandom numbers were used to model these structures.

2.7. Hall Measurements

A Linseis HCS 1 instrument with two permanent magnets (±0.7 T) was used to conduct the Hall effect measurements under an N_2 environment at a temperature range of 40–200 °C.

2.8. Thin Film Thermoelectric Generators

An in-plane π-shaped thermoelectric generator (TEG) was fabricated on an SLG substrate. The TEG comprises 2 pairs of CFS and silver (Ag) legs, electrically connected in series and thermally in parallel, with dimensions sketched in Figure 1a. The CFS legs were deposited using the same experimental conditions as the optimized CFS sample, i.e., Sample 18, as discussed later in the text. The silver legs (contacts) were deposited by thermal evaporation of elemental Ag pellets. The current (I), voltage (V), and power output ($P = VI = RI^2$) were measured by varying the hot side temperature and load resistance using a homemade setup, shown in Figure 1b. During the measurements, an active cooler was employed at the cold end of the TEG, maintaining a stable temperature of ~20 °C, supported on a heat dissipator (passive cooler). Foams were placed to preserve the local temperature on the hot side. Figure 1b also shows the TEG and the circuit employed for the measurement, where a Keithley 2611 A served as the ammeter and voltmeter.

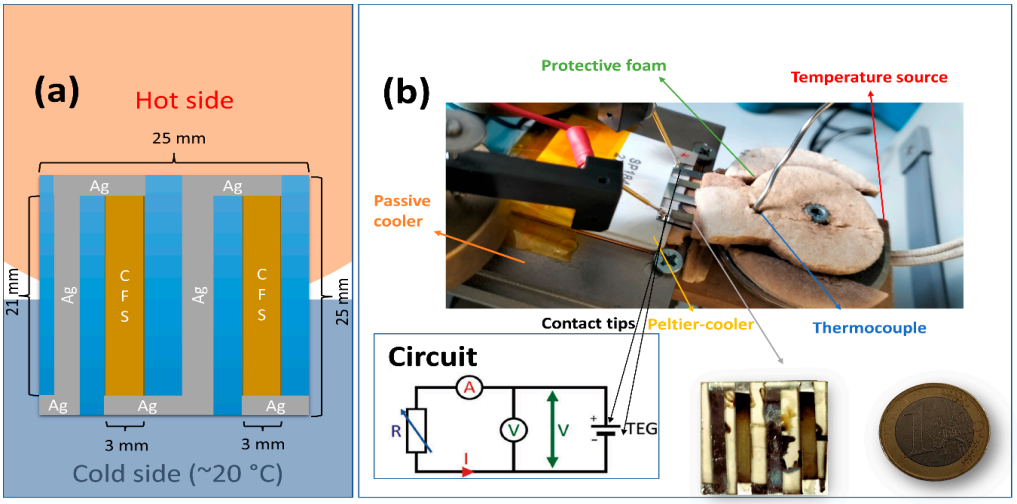

Figure 1. (**a**) TEG dimensions and layout. (**b**) Homemade setup for the I-V-P measurements, circuit diagram, and real-size comparison of the TEG with a one-euro coin for scale.

3. Results

3.1. Evaporation Optimization

3.1.1. Non-Milled Cu-Fe Powder Evaporation

To optimize the CFS thin film deposition, it is necessary to have a prior understanding of the thermal evaporation of the elemental Fe and Cu powders. Therefore, the thermal evaporation was carried out on pristine Fe and Cu, as well as in a manual mix of Fe-Cu powders (atomic ratio 1:1). The XRD patterns of the evaporated films are shown in Figure 2a, and their respective evaporation parameters are summarized in Figure 2b (with full details in Table S2 of the Supplementary Material). Through iterative experimentation, the evaporation current for Cu and Fe was established as 105 A and 140 A for Samples (1) and (2), respectively. The same currents were employed during Cu-Fe blend powder evaporation

for Samples (3) and (4). For Samples (5)–(8), an optimization of the target-to-source distance and current-step variation was performed. Fine details can be found in Supplementary Note S2. Overall, one can notice that the melting point of Fe (1538 °C) is higher than that of Cu (1085 °C), so clearly, compared to Cu (I = 105 A), the evaporation of Fe (I = 140 A) required a higher current. This also means that, during the evaporation process of Cu-Fe mixed powders, Cu evaporates first, forming the base layer of the film, followed by the deposition of Fe, which creates the surface layer (a bilayer film). Consequently, the majority of the film's surface exhibits the *bcc* Fe phase.

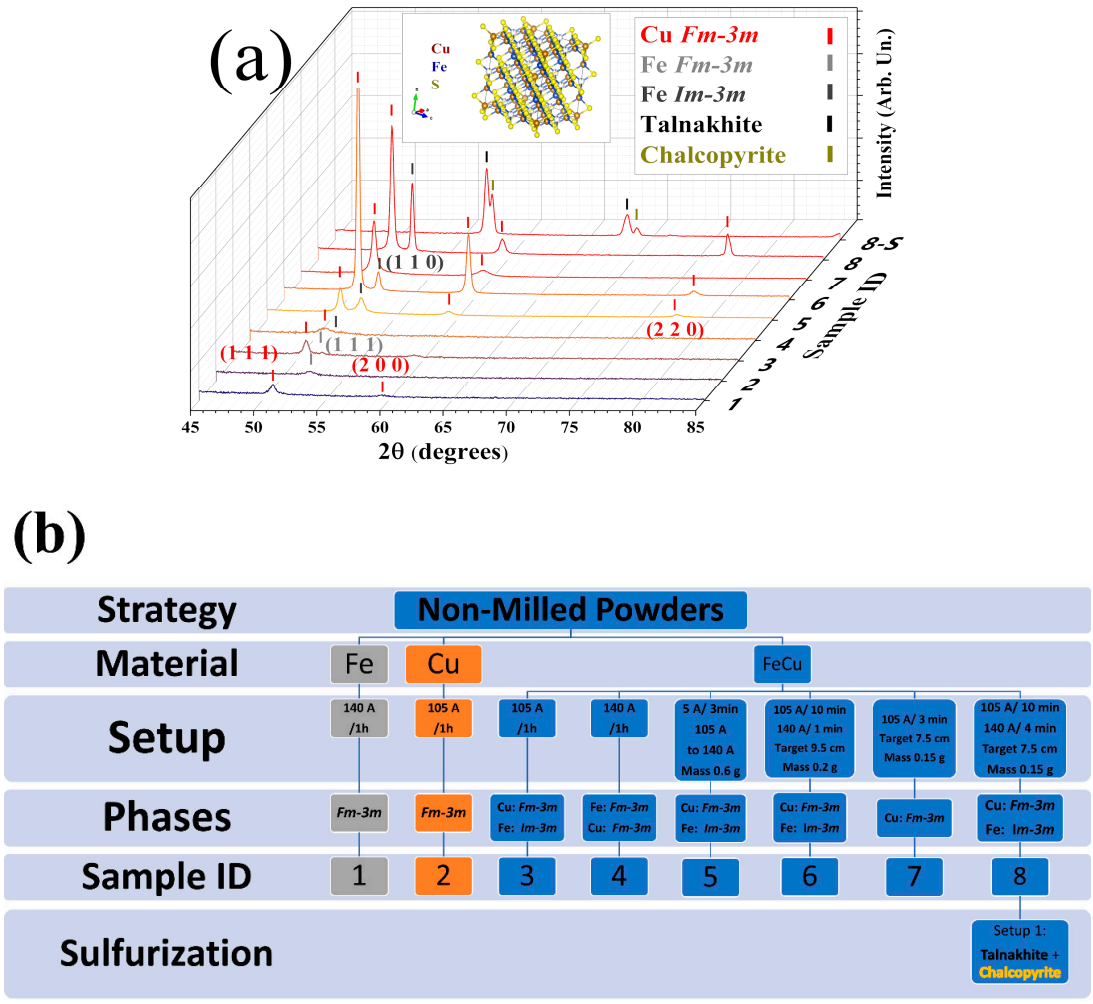

Figure 2. (**a**) Diffractogram of Samples 1 to 8. The tick markers represent the Bragg position of the phases, where the corresponding labeling is in the top-right corner. Sample 8-S represents sulfurized Sample 8, where the process described in Section 2.3 was employed. The inset shows the crystal structure of CFS talnakhite. The Rietveld refinements are available in Supplementary Note S4. (**b**) Diagram with the main synthesis parameters used for the non-milled powder optimization and main results, such as element material used, current employed (A), evaporation time (h), target distance (cm), and mass of powder (g). Please refer to Table S2 for further details.

Among all these tests (Samples 1–8), Sample 8 is the most promising due to a better intermixing of Fe-Cu in the as-evaporated film. Sulfurization of Sample 8 under a static Ar atmosphere resulted in the formation of two phases, namely CFS chalcopyrite (*I-42d*, PDF # 04-002-0241) as the major phase (~70% weight proportion) and a minor $Cu_{18.32}Fe_{15.9}S_4$ talnakhite phase (*I-43m*, PDF # 01-071-2438) with ~30% weight proportion. The talnakhite phase presents low thermal conductivity [10], although in this case, the

mixing of phases turns the sample poor in adhesion, as can be visualized in Figure S22 of the Supplementary Materials.

To gain an insight into the multiphase formation in the thin film, the DFT phase diagram for Cu-Fe-S is presented in Figure 3. The gradient scale shows the formation energy per atom, which is a measure of the energy required to form one unit of the compound from its atoms. The CFS chalcopyrite phase has a formation energy of −0.411 eV/atom, with the talnakhite and bornite phases presenting values of −0.214 eV/atom and −0.090 eV/atom, respectively. Hence, chalcopyrite is the most stable phase among the ternary compounds; however, the proximity in the formation energies of other Cu-Fe-S phases makes it challenging to obtain a pure CFS. Moreover, the binary alloys of FeS_2 and CuS_2 also have low formation energies and are likely to form.

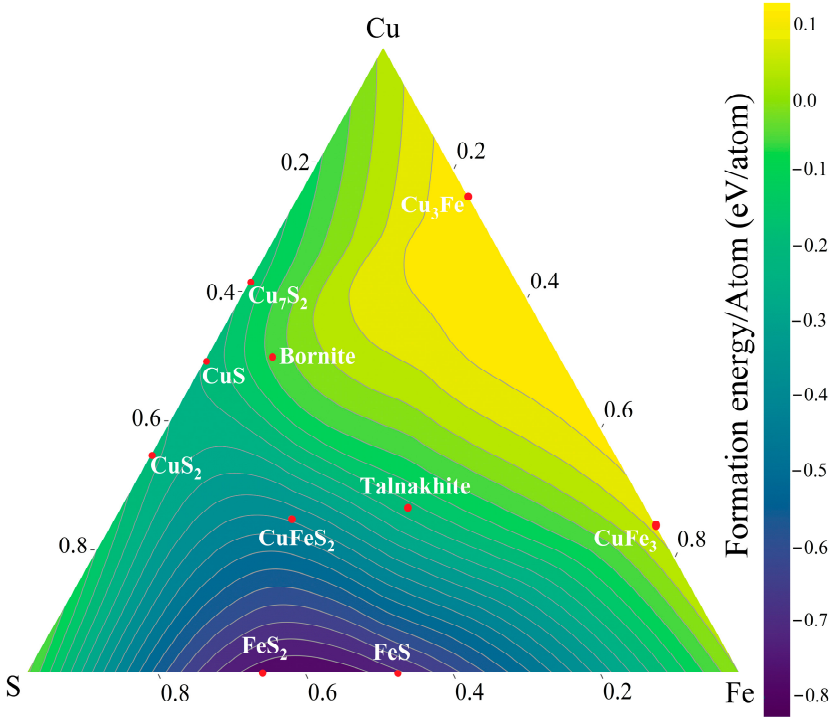

Figure 3. Ternary contour plot of the phase diagram of Cu, Fe, and S obtained through DFT calculations.

In the literature, the Cu-Fe-S phase diagram was summarized in the work of V. Raghavan [35] from experimental information. Indeed, the complexity of the Cu-Fe-S goes beyond what is reported here using DFT, where more than 12 ternary Cu-Fe-S phases are identified to form, and a handful number of secondary phases are made present. However, one can highlight that the studies on the $CuFeS_2$-FeS composite system show the effect of the FeS in the system during heating [36]. $CuFeS_2$ chalcopyrite can only form in a pure phase if the quantity of FeS is below 5% throughout the range of temperature from 400 °C to 550 °C. We speculate that the presence of two distinct layers of Cu and Fe present in the films can induce the formation of Fe sulfide phases. Thus, it indicates that a better intermix of Cu and Fe must be performed. Hence, ball-milling of CuFe can be used to overcome the stoichiometry issue.

3.1.2. Optimization of the Ball-Milled Cu-Fe

A common description of the mechanochemical reaction mechanism for ductile–ductile alloying is given by Suryanarayana [37]. As the milling starts, the ductile materials are subjected to plastic deformation and form bigger agglomerates. With milling time, the grains undergo cold hardening and eventually break, exposing fresh active surfaces. This breaking reduces the grain size and favors the exchange of electrons and ions between the reactants. A further increase in milling time leads to the formation and growth of

short-range crystal order. A complete reaction is only possible if one material successfully diffuses into the other.

For CuFe alloys, M. Rabiee et al. [38] used a shaker mill and suggested that the dissolution of Fe into the Cu requires longer milling times (20 h) compared to those employed here (3 h) for a 20% Fe proportion. However, metastable *fcc* CuFe alloy with 1:1 proportion (desired for $CuFeS_2$) is only achieved by even longer milling times (20–360 h) for both low- and high-energy ball-milling [39,40] or by high-pressure synthesis [41,42]. Even upon completion, when thermally treated, CuFe alloys remain metastable and tend to decompose back into separate Cu and Fe phases [43,44]. However, the mechanisms of milling, such as plastic deformation, agglomeration, and nucleation, can still be used to better intermix Cu and Fe for evaporation, even if the formation of the CuFe alloy is not complete. Milling can also tackle another problem observed during the evaporation of the metal precursors. As discussed earlier (Samples 3–7), the evaporation of non-milled power results in bilayer films, where the ferromagnetic properties of *fcc* Fe cause significant damage to the film surface (see Figure S23).

Therefore, three different milling conditions were tested, as described in Section 2.1 and Table S1. The first (FeCu-01) and second ($Fe_{1.76}$Cu-02) samples were milled for 2 h, with Fe:Cu ratios of 1:1 and 1.76:1, respectively. The third sample (with Fe:Cu = 1:1) was milled for 3 h using ethanol as a control process agent. The XRD patterns of the three as-milled Fe-Cu powders are shown in Figure 4. The Rietveld refinements (see Figures S18–S20 of the Supplementary Materials) show that the $Cu_{0.8}Fe_{0.2}$ (PDF4+ database entry #40031453) gives a good fit for the diffractograms for the three different samples. However, the Cu:Fe proportion might not be 0.8:0.2 for all of them. Since Cu and Fe have a similar number of electrons, this ratio is hard to correctly retrieve using XRD; however, the incorporation of Fe into the structure can be seen by the decrease in the Fe relative intensities of samples FeCu-01 and FeCu-03. This is also observed in an increase in the lattice parameters from FeCu-01 to Fe1.76Cu-02, and to FeCu-03 of 3.6197(3) Å, 3.628(4) Å, and 3.640(4) Å, respectively.

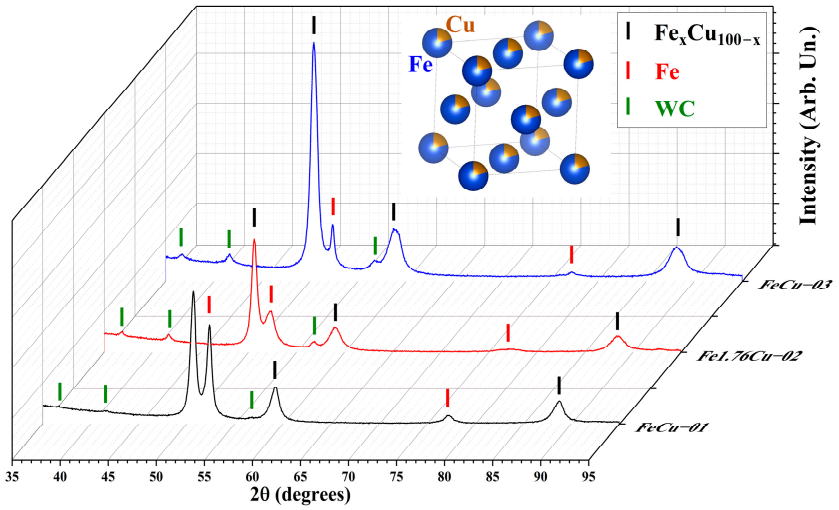

Figure 4. Diffractograms of the FeCu-01, $Fe_{1.76}$Cu-02, and FeCu-03 ball-milled powders. Rietveld refinements are available in Figures S18–S20. The tick markers indicate the Bragg 2θ positions of the Fe_xCu_{100-x} fcc phase (black, PDF4+ database entry #40031453), Fe bcc (red, PDF4+ database entry #40079753), and WC (green, PDF4+ database entry #40045823).

In order to investigate the effect of milling in evaporation, the first tests using the FeCu-01 milled powders were performed for Samples 9–11. All the strategies use a stepwise increase in current (see Table S2 for reference). The diffractograms for these samples are shown in Figure 5a, and the main parameters of synthesis are found in Figure 5b. The strategy now consists of optimizing the source-to-target distance. Comparing Sample 9 (27 cm)

and Sample 10 (7.5 cm), the crystallinity of the as-evaporated films is improved, although the adhesion is still poor. Good adhesion is only achieved when the vacuum is improved, down to 10^{-6} mbar for Sample 11. In these cases, the mass of the powder was also reduced to 0.06 g, increasing the energy per gram of material during evaporation. Further details on this optimization process can be found in Supplementary Note S3.1.

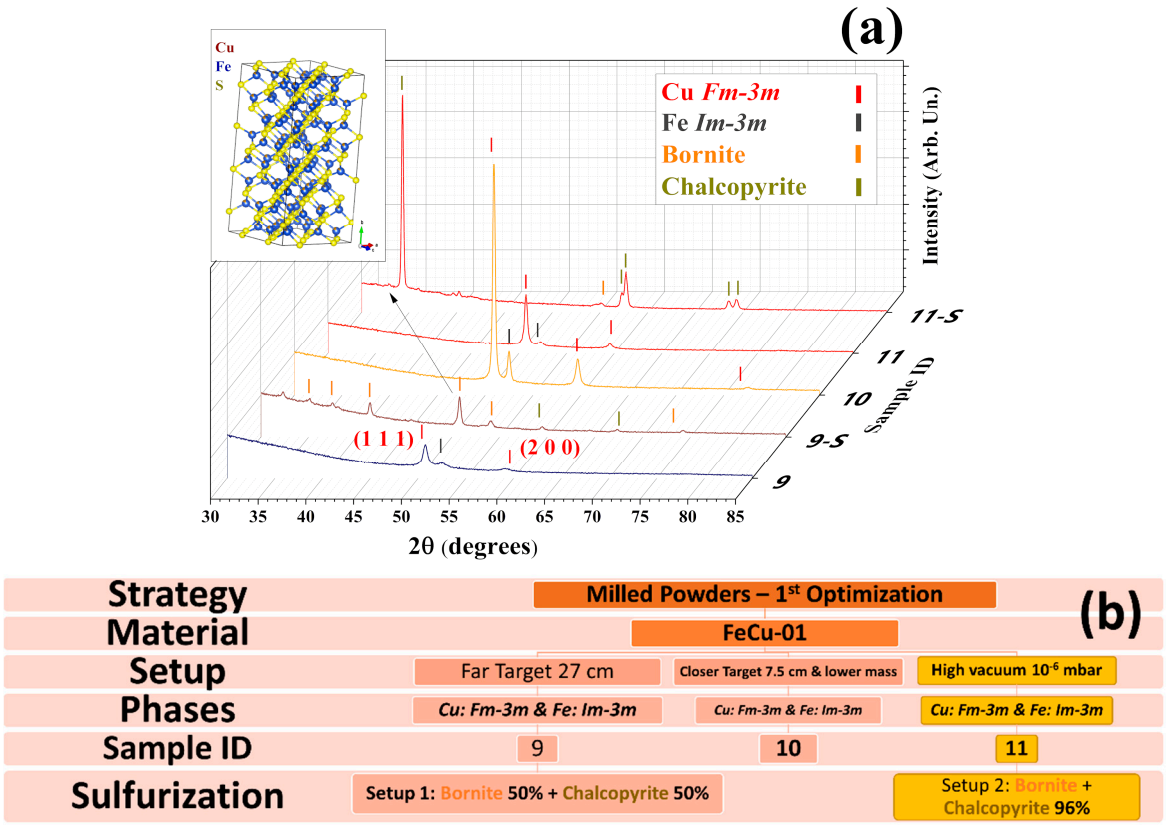

Figure 5. (**a**) Diffractograms for 9 to 11. Samples 9-S and 11-S correspond to the patterns of the sulfurized samples 8 and 11, respectively. The tick markers correspond to the Bragg peaks of the phases identified in the top-right corner, and the Rietveld refinements are available in Supplementary Note S4. (**b**) Diagram with the main synthesis parameters used for the non-milled powder optimization, such as element material used, current employed (A), evaporation time (h), target distance (cm), and mass of powder (g). Please refer to Table S2 for further details.

The sulfurization of Samples 9 and 11 presented bornite $Cu_{4.98}Fe_{1.02}S_4$ (*Pbca*, PDF # 01-071-368, inset of Figure 5a) and CFS chalcopyrite (PDF # 00-037-0471) in different proportions. The quantitative phase analysis (QPA) revealed a higher weight fraction of the CFS phase for Sample 11 (96%), as can also be observed in its visual aspect in Figure S25. Moreover, Sample 11 showed a strong preferred orientation towards [112], [213], and [105] directions (see Figure S11 for Rietveld analysis). The use of setup 2 for the sulfurization, with a dynamic flow of N_2, brings better results compared to setup 1, when a static Ar atmosphere is employed. Thus, Sample 11 presents the best conditions for ball-milled powder evaporation.

Considering the evaporation conditions of Sample 11 (using FeCu-01), the other two as-milled powders ($Fe_{1.76}$Cu-02 and FeCu-03) were evaporated. Figure 6a displays diffractograms of the sulfurized films prepared using the three different milled powders. Figure 6b presents the main parameters utilized. In certain samples marked with the letter P, sandpaper was used to polish the SLG substrates before the evaporation. All the as-evaporated films exhibited *fcc* Cu and *bcc* Fe phases (refer to Figure S29 of Supplementary Note S6). The effect of the polishing can be observed by comparing Samples 12 and 13 in

Figure S26. Overall, this strategy leads to better crystallization and weaker preferred orientation in the post-sulfurized films. However, to make a balance between purity and adhesion quality, Sample 16, without polishing, was selected as the optimized film (see Figure 6a insets). More details regarding the optimization process can be found in Supplementary Note S3.2.

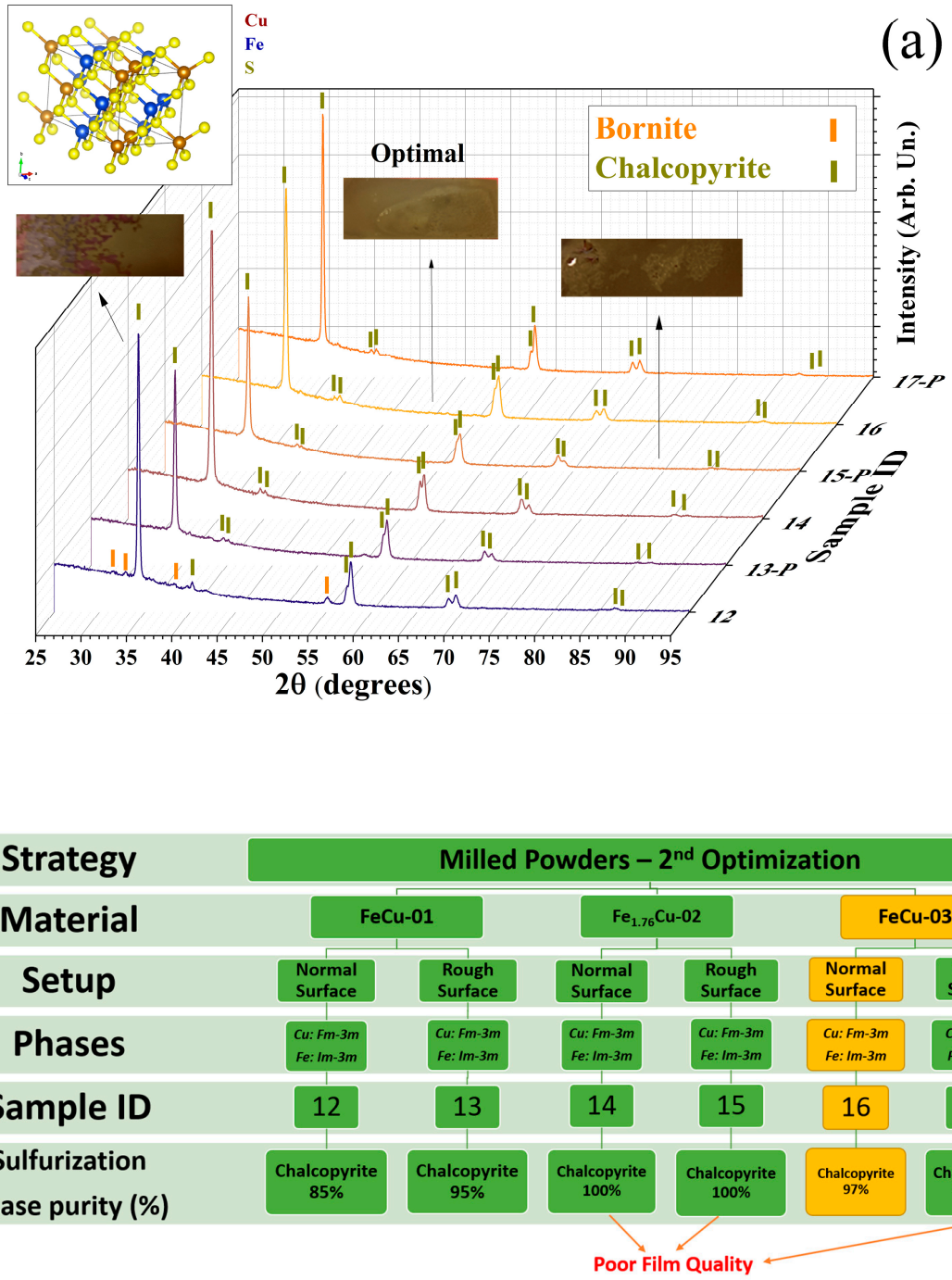

Figure 6. (**a**) Diffractograms of Samples 12 to 17. The P index in the sample ID represents the polishing procedure. The markers identify the main Bragg peaks of the chalcopyrite (yellow) and bornite phases (orange). The inset shows the crystalline structure of CFS-chalcopyrite. In blue are displayed the phase percentages of chalcopyrite in the film. (**b**) Diagram with the syntheses parameters, including the milled powder employed, the strategy of polishing (rough surface), the crystalline phases obtained, and the phase purity of the chalcopyrite phase after sulfurization.

3.2. Optimized CFS Thin Film

To assess the reproducibility of the synthesis, Sample 18 was synthesized with the identical conditions as Sample 16, i.e., evaporating FeCu-03 ball milled powders with a lower vacuum (10^{-6} mbar), using a two-step current of 105 A and 140 A, followed by sulfurization with a dynamic N_2 flow. Further characterization of surface and cross-section morphology, resistivity, carrier concentration, and mobility was carried out on this sample.

Figure 7 shows the Rietveld refinement of the XRD data of Sample 18. The QPA shows that the sample consists mainly of the desired CFS chalcopyrite phase (PDF # 000250288), ~93% by weight. Nevertheless, the CuFe-bornite (PDF #40080243) and pyrite FeS_2 (PDF #000060710) phases also formed along with CFS, with a weight percentage of ~5 and 2%, respectively. The chalcopyrite phase also shows a preferred orientation along the [112] direction. Good agreement is observed for the profile fitting and experimental data, as shown by the featureless residual curve. Since FeS_2 requires the lowest formation energy among the different Cu-Fe-S phases (see Figure 3), its presence as a secondary phase is also expected. As is common for thin films, the contribution of crystallite size is better represented by a Gaussian profile function, which yields a volumetric crystallite size average (L_{vol}) of 61(1) nm. A relatively small microstrain of 0.4(9)% is observed for the chalcopyrite phase, with a predominant Lorentzian contribution to the line profile, see Figure 7.

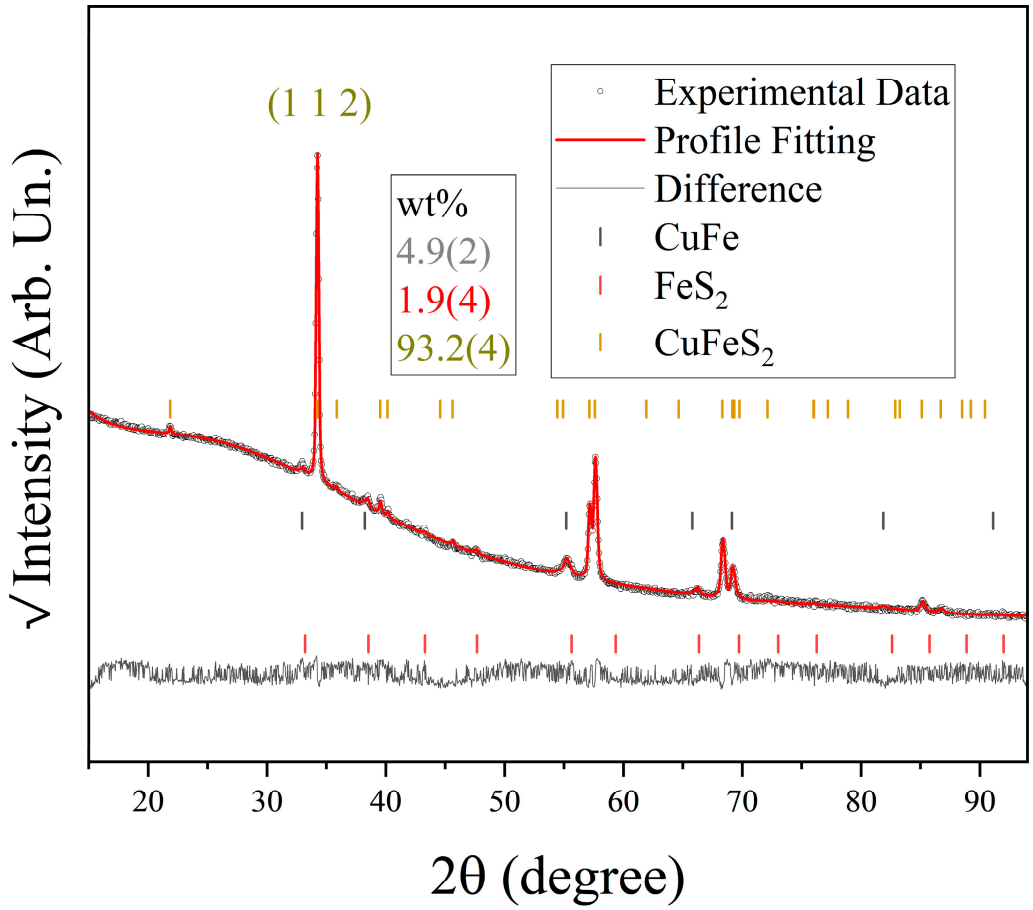

Figure 7. XRD pattern of the CFS-18 sample. Black dots stand for the experimentally obtained data in square root scale, while the red line represents the profile fitting. The grey line shows the residual (difference between the experimental and fitted model). The tick markers represent the Bragg reflections shown in the caption. (1 1 2) is the preferred orientation of CFS chalcopyrite.

The SEM and EDXS analyses of the sulfurized Sample 18 are summarized in Figure 8. On the surface of the film, micrometer-sized grains form bigger polycrystalline agglomerates with an irregular plated shape microstructure (Figure 8a). Figure S31 shows that this morphology is extended throughout a large area of the sample. The chemical maps collected on the same surface suggest that Cu is homogeneously distributed throughout the sample, whereas Fe and S are more distinguished on the top surface of the grains. This reveals that even when the precursor powders are well mixed by the milling procedure, Cu tends to form the base layer of the film when evaporated, leaving the film surface Fe-rich. This also corroborates the slightly Fe-rich stoichiometry observed in the crystalline phases obtained using XRD.

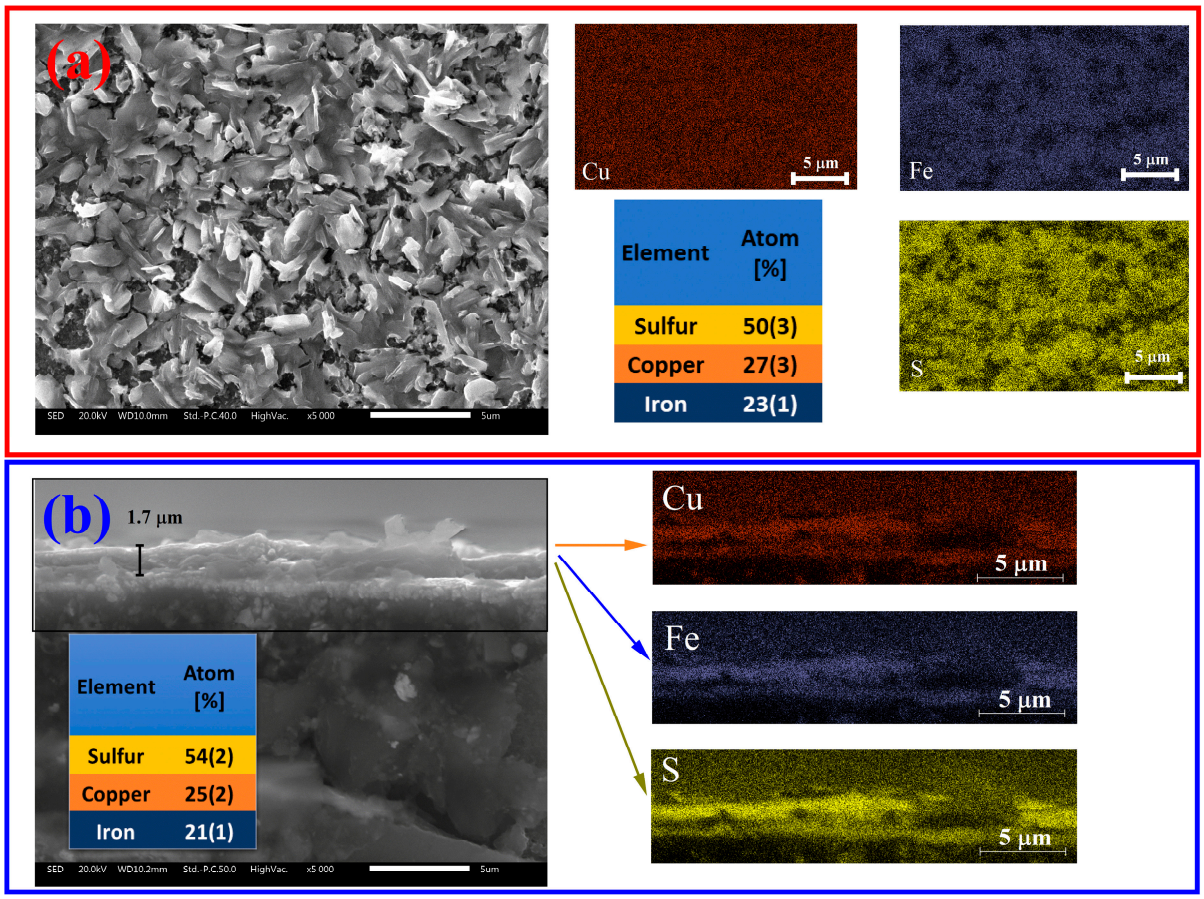

Figure 8. SEM and EDXS analysis of Sample 18. (**a**) Surface scan (**left**), EDXS and chemical mapping (**right**). The table contains information on EDXS analysis of the atomic proportion of each element. (**b**) Cross section of the thin film.

SEM and EDXS measurements of the CuFe precursor (FeCu-03, pre-sulfurized Sample 18) can be visualized in Supplementary Note S7. This film shows a smooth and clean surface morphology, with a slightly copper-rich stoichiometry on the surface. For the CFS film, the average thickness is ~1.7 µm, as seen in the cross-section micrograph of Figure 8b, left. The cross-section of the film is also Cu-rich, adding to the fact that it forms the base layer of the film.

The electrical characterization of the sulfurized Sample 18 is shown in Figure 9. The conductivity of the CFS film increases with the temperature, and carrier concentration shows a positive value, confirming a non-degenerate *p*-type semiconductor nature. To explain the *p*-type nature, we see that Cu is forming as the base layer of the film, and CFS is believed to be Fe-rich. Since the oxidation state of CFS is often understood as $Cu^{+}Fe^{3+}S_2^{2-}$, the *p*-type nature of CFS can be stabilized by substituting Cu^{1+} with Fe^{3+} or, in general, by

reducing the valence of the cations or by increasing the valence of the anions [45]. The Hall measurement reveals that the carrier concentration does not show significant temperature variation, which is consistent with previous reports on this material (1.8×10^{19} cm^{-3}) [45]. Furthermore, the carrier concentration is in the same order of magnitude and the mobility is reduced from the literature values, which can be credited to the morphology of the sample. This affects the overall conductivity, which tends to be lower than the literature-reported values for *p*-type CFS [26,45].

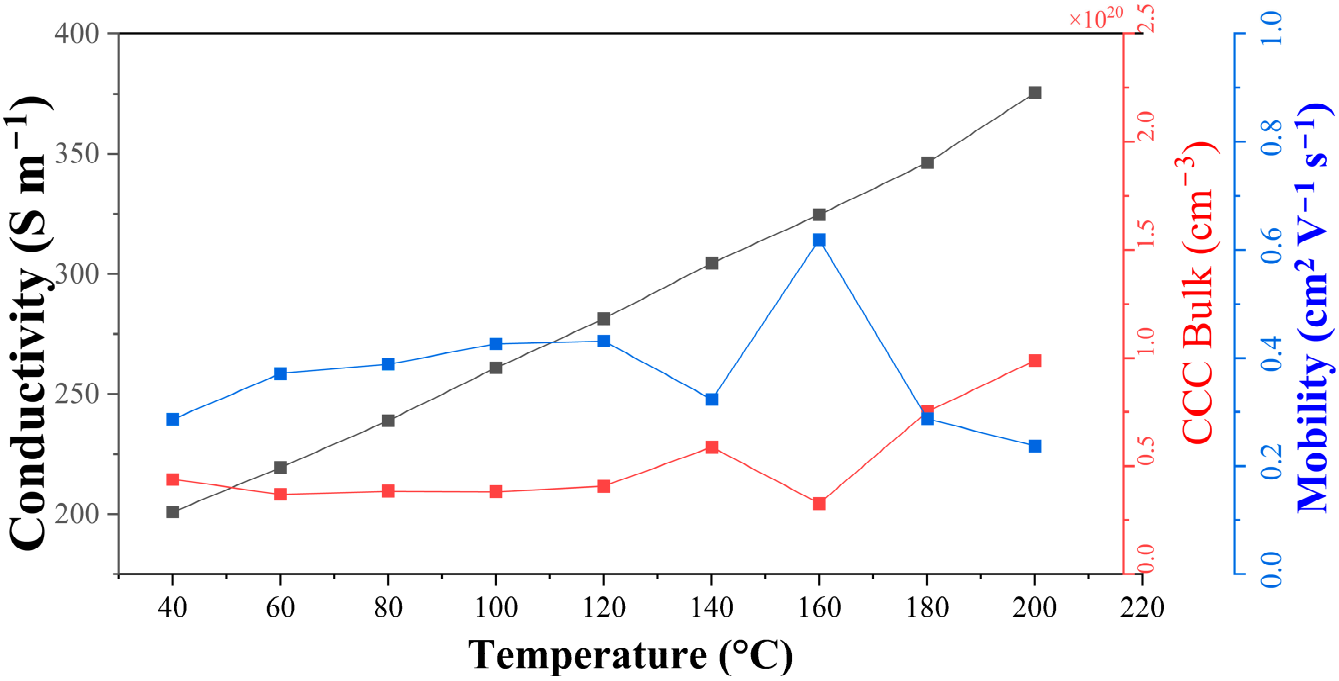

Figure 9. Electronic characterization of the CFS-18 samples with increasing temperature. The electrical conductivity is displayed in black squares (left axis), charge carrier concentration (CCC) in red, and electron mobility in blue, both in the right axis.

An in-plane TEG was fabricated with two couples of CFS and Ag legs. The two CFS legs were deposited following the optimized evaporation and sulfurization parameters of Sample 18, as illustrated in Figure 1a. The current and voltage output data, shown in Figure 10a, were collected using a homemade setup (Figure 1b) by varying the hot side temperature from 50 °C to 200 °C. In this temperature span, the TEG shows an open circuit voltage (VOC) varying from 3 to 80 mV and a short circuit (SC) current from 1 to 7.7 µA. The current–voltage–power (I-V-P) curves are shown in Figure 10b. For a temperature difference (ΔT) of 180 °C, a maximum power of 171 nW was obtained by applying a load resistance of 5 kΩ. More convenient ways to express the performance rely on dividing the power output by units of total, active, or cross-sectional areas of the generator [19]. Here, the total denotes the entire surface area of the TEG, and the actual area refers to the specific region where the CFS material is present. The thickness of the material is measured using a profilometer, and the cross-sectional area is obtained by multiplying it by the width of the film. Per unit of total area, the performance reads 27 nW cm^{-2}; in units of active area, 114 nW cm^{-2}; and in cross-sectional area, 4 mW cm^{-2}.

The power output results are higher compared to some of the eco-friendly TEGs fabricated using hot injection and ball-milled inks. Cu_2SnS_3, Cu_2ZnSnS_4, $Cu_{2.124}Zn_{0.875}SnS_3Se$ TEGs, for example, presented a power output per unit of active area of 59 nW cm^{-2}, 43 nW cm^{-2}, 23 nW cm^{-2}, respectively, at a $\Delta T = 160$ °C [20]. The better homogeneity of the film provided by the three-step method can be the reason for the superior performance. However, a fair comparison can only be made between similar materials, and, to the best of our knowledge, no device made of CFS was reported in the literature. The values

reported here are still lower than the optimized TEGs for $Cu_{2+x}Zn_{1-x}SnS_4$ (152 nW cm^{-2}) and $Cu_{2+x}Zn_{1-x}SnSe_4$ (279 nW cm^{-2}) at a $\Delta T = 150$ °C, produced by sputtering [19]. It is important to notice that the TEG presented in this work is a proof-of-concept device fabricated using a noble approach where the CFS legs were deposited using the three-step method. The optimization of the CFS TEG can lead to a further enhancement in overall power output.

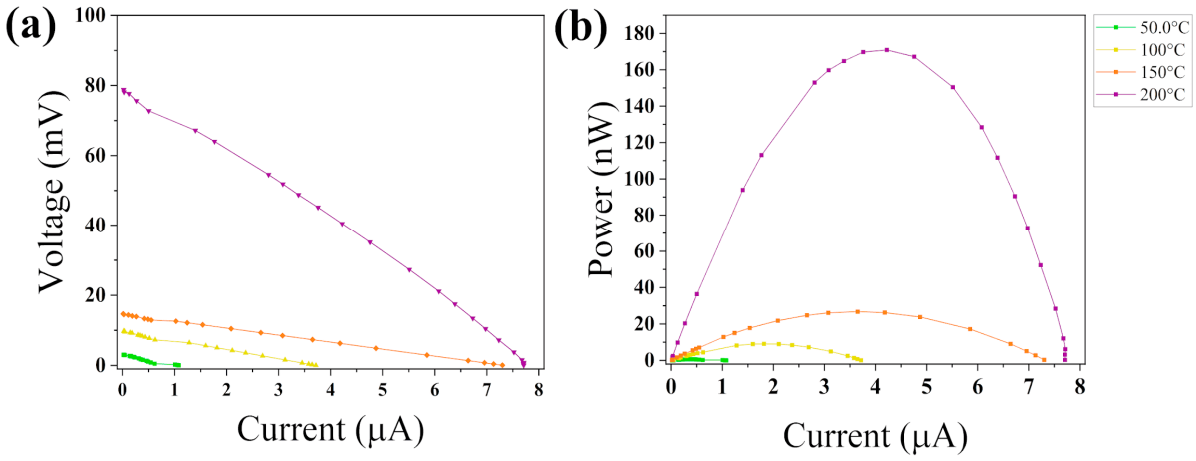

Figure 10. (**a**) I-V plots and (**b**) I-V-P output measurements for the CFS TEG. The temperature depicted in the figure corresponds to the hot side, while a passive cooler was employed on the cold side to maintain a temperature of approximately 20 °C.

4. Discussion

In this study, we present a comprehensive analysis of the three-step synthesis of CFS, examining its physical and chemical properties. Moreover, we demonstrate its successful application as a thermoelectric generator, yielding a power output comparable to similar chalcogenide-based materials [20,46–50]. Comparing our proposed three-step method with existing literature can offer valuable insights into the potential applications of CFS chalcopyrite beyond thermoelectricity.

The predominant technique for producing bulk polycrystalline CFS involves wet-chemical reactions [13,14,51–57]. This route provides control over its nanoscale dimensions, enabling the tunning of its optical properties and exploring the quantum confinement effect. The polycrystalline nature also results in a higher surface-area-to-volume ratio for the material, promoting additional active sites for electrocatalysis applications [58]. Another notable attribute of CFS is its robust electrochemical stability, enabling it to endure repeated recharging cycles in battery systems [59,60]. Furthermore, this stability has been harnessed in various applications, including its role as an electrode material for electrocatalytic oxygen reduction in fuel cells and water electrolyzers [58]. It also emerges as a promising alternative to platinum as counter electrodes in dye-sensitized solar cells [61].

The synthesis method provided here does not achieve precise control over the microstructure, although a nano flower-like morphology is observed (see Figure 8a). Examples of similar materials with a plate-like structure have been demonstrated by Sathyaseelan et al. [62], Ding et al. [59], and Li et al. [63] as advantageous for electrochemical, Li-ion battery cathode and magnetic applications due to its high surface-area-to-volume ratio. The difference between the three-step method compared to the above-mentioned wet-chemical process is that it is a dry route, with no need for washing processes and the complete absence of wet chemical contaminations. However, further studies must be performed to check the stability under the aqueous (electrolyte solution) environment from our samples for electrocatalytic (battery) applications.

For thermal evaporation, Barkat et al. [27] adopted a similar synthesis route compared to the present work. They heated the substrate during the evaporation to increase the

diffusion of Fe into Cu instead of ball-milling. The control of stoichiometry is similar to what is reported here, although the plate-like morphology was absent. Therefore, the microstructure of the CFS film can be extremely diverse if milling is employed before powder evaporation and offers a simple alternative for improving Fe-Cu diffusion. Moreover, the inclusion of a ball-milling step before evaporation showed the formation of three distinct Cu-Fe-S phases. We put forward that by fine-tuning specific synthesis parameters, these phases can be obtained separately. Additionally, the parameters of milling can be tuned to regulate the Cu:Fe proportion in CFS, especially if aiming to modify its electrical properties from *p* to *n*-type nature.

5. Conclusions

This study presents a novel method to fabricate $CuFeS_2$ chalcopyrite thin films using a three-step synthesis of ball-milling, thermal evaporation, and sulfurization. We can emphasize some points of the optimization process: (1) ball-milling the metallic precursors before evaporation is essential for effective Cu and Fe element mixing; (2) a two-step current of 105 A (for 10 min) and 140 A (for 1 min) is required due to the different melting points of Cu and Fe; (3) using a smaller quantity of mass can improve the energy-over-mass ratio during evaporation; (4) high vacuum (~10^{-6} mbar) and proximity between source and target enhance film adhesion. Finally, the sulfurization requires vacuuming the furnace and sintering at 425 °C for 1 h under dynamic N_2 flow. The optimized thin film exhibits a plate-like surface morphology and demonstrates *p*-type semiconducting behavior with a purity of 93% for the CFS chalcopyrite phase. These features can be used for electrochemical applications, although further tests are needed to verify the stability of the material under an aqueous/electrolyte environment. Additionally, we observed the formation of bornite and talnakhite phases during the optimization process. This is likely because their energy phase formation is similar to that of CFS, as determined by DFT phase-diagram calculations. We suggest that this three-step approach can synthesize these ternary phases in pure form by making specific adjustments to the synthesis parameters. A proof-of-concept CFS-based in-plane TEG fabricated using the optimized thin film showed a power output per unit active area of ~114 nW cm^{-2} for a temperature gradient of ~180 °C. The performance is superior to other sulfide-based materials fabricated using ball-milling and hot injection inks due to the smaller thickness and uniformity of the thin film. However, no CFS TEG performance was reported for a direct comparison. Further studies on the CFS material's properties, such as the Seebeck coefficient, electrical resistivity, and thermal conductivity, are required to understand the effect of thickness on the overall TE performance of the thin film. In short, this work provides a comprehensive step-by-step guide to fabricating CFS thin films and opens avenues to use this eco-friendly, stable, cost-effective, and sustainable material for diverse applications.

Supplementary Materials: The following supporting information can be downloaded at https://www.mdpi.com/article/10.3390/app131810172/s1, Figure S1 to Figure S20: Rietveld refinements of the thin film XRD for all the samples; Figure S21 to Figure S31: pictures of the thin films for visual inspection; Figure S32: XRD patterns of the as-deposited CuFe thin films; Figure S33: SEM and EDX analysis of the as-deposited CuFe thin films; Figure S34: SEM micrograph of Sample 18; Table S1: Ball-milling parameters; Table S2: Thermal evaporation parameters.

Author Contributions: Conceptualization, N.A. and P.S.; Methodology, M.A.M., M.D. and N.A.; Software, H.N.; Validation, N.A.; Formal analysis, K.L.; Investigation, M.D., H.N. and N.A.; Resources, M.D. and N.A.; Writing—original draft, M.A.M.; Writing—review & editing, M.A.M., K.L. and H.N.; Supervision, N.A. and P.S.; Project administration, P.S.; Funding acquisition, P.S. All authors have read and agreed to the published version of the manuscript.

Funding: University of Trento: Department Strategic Plan 2022-2024.

Institutional Review Board Statement: Not applicable.

Data Availability Statement: The data presented in this study are available on request from the corresponding author.

Acknowledgments: Robert Dinnebier and Sebastian Bette are acknowledged for useful discussion regarding DFT calculations aided by the HAWK supercomputer within the Diskete Project framework.

Conflicts of Interest: The authors declare no conflict of interest.

References

1. Elalfy, L.; Music, D.; Hu, M. Metavalent bonding induced abnormal phonon transport in diamondlike structures: Beyond conventional theory. *Phys. Rev. B* **2021**, *103*, 75203. [CrossRef]
2. Yu, H.; Chen, L.-C.; Pang, H.-J.; Qiu, P.-F.; Peng, Q.; Chen, X.-J. Temperature-dependent phonon anharmonicity and thermal transport in CuInTe. *Phys. Rev. B* **2022**, *105*, 245204. [CrossRef]
3. Wang, C.; Ma, Q.; Xue, H.; Wang, Q.; Luo, P.; Yang, J.; Zhang, W.; Luo, J. Tetrahedral distortion and thermoelectric performance of the Ag-substituted $CuInTe_2$ chalcopyrite compound. *ACS Appl. Energy Mater.* **2020**, *3*, 11015–11023. [CrossRef]
4. Wang, K.; Qin, P.; Ge, Z.H.; Feng, J. Highly enhanced thermoelectric properties of p-type $CuInSe_2$ alloys by the Vacancy Doping. *Scr. Mater.* **2018**, *149*, 88–92. [CrossRef]
5. Minerals, R. Chalcopyrite—$CuFeS_2$. *Dev. Econ. Geol.* **1975**, *4*, 242–253. [CrossRef]
6. Xie, H.; Su, X.; Hao, S.; Zhang, C.; Zhang, Z.; Liu, W.; Yan, Y.; Wolverton, C.; Tang, X.; Kanatzidis, M.G. Large Thermal Conductivity Drops in the Diamondoid Lattice of $CuFeS_2$ by Discordant Atom Doping. *J. Am. Chem. Soc.* **2019**, *141*, 18900–18909. [CrossRef]
7. Sato, N.; Gan, P.S.; Tsujii, N.; Mori, T. Effect of microstructure on lattice thermal conductivity of thermoelectric chalcopyrite $CuFeS_2$: Experimental and computational studies. *Appl. Phys. Express* **2021**, *14*, 087002. [CrossRef]
8. Long, S.O.J.; Powell, A.V.; Vaqueiro, P.; Hull, S. High Thermoelectric Performance of Bornite through Control of the Cu(II) Content and Vacancy Concentration. *Chem. Mater.* **2018**, *30*, 456–464. [CrossRef]
9. Qiu, P.; Zhang, T.; Qiu, Y.; Shi, X.; Chen, L. Sulfide bornite thermoelectric material: A natural mineral with ultralow thermal conductivity. *Energy Environ. Sci.* **2014**, *7*, 4000–4006. [CrossRef]
10. Mukherjee, S.; Powell, A.V.; Voneshen, D.J.; Vaqueiro, P. Talnakhite: A potential n-type thermoelectric sulphide with low thermal conductivity. *J. Solid State Chem.* **2022**, *314*, 123425. [CrossRef]
11. Pang, H.; Bourgès, C.; Jha, R.; Baba, T.; Sato, N.; Kawamoto, N.; Baba, T.; Tsujii, N.; Mori, T. Revealing an elusive metastable wurtzite $CuFeS_2$ and the phase switching between wurtzite and chalcopyrite for thermoelectric thin films. *Acta Mater.* **2022**, *235*, 118090. [CrossRef]
12. Li, J.; Tan, Q.; Li, J.-F. Synthesis and property evaluation of $CuFeS_{2-x}$ as earth-abundant and environmentally-friendly thermoelectric materials. *J. Alloy. Compd.* **2013**, *551*, 143–149. [CrossRef]
13. Liang, D.; Ma, R.; Jiao, S.; Pang, G.; Feng, S. A facile synthetic approach for copper iron sulfide nanocrystals with enhanced thermoelectric performance. *Nanoscale* **2012**, *4*, 6265–6268. [CrossRef]
14. Vaure, L.; Liu, Y.; Cadavid, D.; Agnese, F.; Aldakov, D.; Pouget, S.; Cabot, A.; Reiss, P.; Chenevier, P. Doping and Surface Effects of $CuFeS_2$ Nanocrystals Used in Thermoelectric Nanocomposites. *ChemNanoMat* **2018**, *4*, 982–991. [CrossRef]
15. Tsujii, N.; Mori, T. High Thermoelectric Power Factor in a Carrier-Doped Magnetic Semiconductor $CuFeS_2$. *Appl. Phys. Express* **2013**, *6*, 043001. [CrossRef]
16. Tsujii, N. Possible enhancement of thermoelectric properties by use of a magnetic semiconductor: Carrier-doped chalcopyrite $Cu_{1-x}Fe_{1+x}S_2$. *J. Electron. Mater.* **2013**, *42*, 1974–1977. [CrossRef]
17. Xie, H.; Su, X.; Zheng, G.; Zhu, T.; Yin, K.; Yan, Y.; Uher, C.; Kanatzidis, M.G.; Tang, X. The Role of Zn in Chalcopyrite $CuFeS_2$: Enhanced Thermoelectric Properties of $Cu_{1-x}Zn_xFeS_2$ with In Situ Nanoprecipitates. *Adv. Energy Mater.* **2017**, *7*, 1601299. [CrossRef]
18. Nolas, G.S.; Sharp, J.; Goldsmid, H.J. The Phonon—Glass Electron-Crystal Approach to Thermoelectric Materials Research. In *Thermoelectrics*; Springer: Berlin/Heidelberg, Germany, 2001; pp. 177–207. [CrossRef]
19. Isotta, E.; Andrade-Arvizu, J.; Syafiq, U.; Jiménez-Arguijo, A.; Navarro-Güell, A.; Guc, M.; Saucedo, E.; Scardi, P. Towards Low Cost and Sustainable Thin Film Thermoelectric Devices Based on Quaternary Chalcogenides. *Adv. Funct. Mater.* **2022**, *32*, 2202157. [CrossRef]
20. Syafiq, U.; Isotta, E.; Ataollahi, N.; Lohani, K.; Luong, S.; Trifiletti, V.; Fenwick, O.; Scardi, P. Facile and Low-Cost Fabrication of Cu/Zn/Sn-Based Ternary and Quaternary Chalcogenides Thermoelectric Generators. *ACS Appl. Energy Mater.* **2022**, *5*, 5909–5918. [CrossRef]
21. Tsujii, N.; Mori, T.; Isoda, Y. Phase stability and thermoelectric properties of $CuFeS_2$-based magnetic semiconductor. *J. Electron. Mater.* **2014**, *43*, 2371–2375. [CrossRef]
22. Sato, K.; Teranishi, T. Optical absorption of a thin $CuFeS_2$ film. *J. Phys. Soc. Jpn.* **1976**, *40*, 197–298. [CrossRef]
23. Korzun, B.; Galyas, A. Thin Films of $CuFeS_2$ Prepared by Flash Evaporation Technique and Their Structural Properties. *J. Electron. Mater.* **2019**, *48*, 3351–3354. [CrossRef]
24. Khalid, M.A.; Salim, I.K. Optical and DC Electrical Investigations of $CuFeS_2$ Thin Films Prepared by Spray Pyrolysis Technique. *J. Basrah Res.* **2007**, *33*, 43–53.

25. Rouchdi, M.; Mamori, H.; Salmani, E.; Ait Syad, B.; Mounkachi, O.; Essajai, R.; Ez-zahraouy, H.; Chakchak, H.; Hassanain, N.; Benyoussef, A.; et al. Physicochemical characterization and catalytic performance of Fe doped CuS thin films deposited by the chemical spray pyrolysis technique. *Appl. Phys. A Mater. Sci. Process.* **2021**, *127*, 441. [CrossRef]
26. Rana, T.R.; Khadka, D.B.; Kim, J. Sulfur stoichiometry driven chalcopyrite and pyrite structure of spray pyrolyzed Cu-alloyed FeS_2 thin films. *Mater. Sci. Semicond. Process.* **2015**, *40*, 325–330. [CrossRef]
27. Barkat, L.; Hamdadou, N.; Morsli, M.; Khelil, A.; Bernède, J.C. Growth and characterization of $CuFeS_2$ thin films. *J. Cryst. Growth* **2006**, *297*, 426–431. [CrossRef]
28. Levin, I. *NIST Inorganic Crystal Structure Database (ICSD)*; National Institute of Standards and Technology: Gaithersburg, MD, USA, 2018. [CrossRef]
29. Gates-Rector, S.; Blanton, T. The Powder Diffraction File: A quality materials characterization database. *Powder Diffr.* **2019**, *34*, 352–360. [CrossRef]
30. Coelho, A.A. TOPAS and TOPAS-Academic: An optimization program integrating computer algebra and crystallographic objects written in C++. *J. Appl. Crystallogr.* **2018**, *51*, 210–218. [CrossRef]
31. Black, D.R.; Mendenhall, M.H.; Brown, C.M.; Henins, A.; Filliben, J.; Cline, J.P. Certification of Standard Reference Material 660c for Powder Diffraction. *Powder Diffr.* **2020**, *35*, 17–22. [CrossRef]
32. Kresse, G.; Furthmüller, J. Efficient Iterative Schemes for Ab Initio Total-Energy Calculations Using a Plane-Wave Basis Set. *Phys. Rev. B* **1996**, *54*, 11169. [CrossRef]
33. Kresse, G.; Furthmüller, J. Efficiency of Ab-Initio Total Energy Calculations for Metals and Semiconductors Using a Plane-Wave Basis Set. *Comput. Mater. Sci.* **1996**, *6*, 15–50. [CrossRef]
34. Perdew, J.P.; Burke, K.; Ernzerhof, M. Generalized Gradient Approximation Made Simple. *Phys. Rev. Lett.* **1996**, *77*, 3865–3868. [CrossRef]
35. Raghavan, V. Cu-Fe-S (Copper-Iron-Sulfur). *J. Phase Equilibria Diffus.* **2004**, *25*, 450–454. [CrossRef]
36. Ueno, T.; Kitakaze, A.; Sugaki, A. Phase Relations in the $CuFeS_2$-FeS Join. *Sci. Rep. Tohuku Univ. Ser.* **1980**, *16*, 283–293.
37. Suryanarayana, C. Mechanical alloying and milling. *Prog. Mater. Sci.* **2001**, *46*, 1–184.
38. Rabiee, M.; Mirzadeh, H.; Ataie, A. Processing of Cu-Fe and Cu-Fe-SiC nanocomposites by mechanical alloying. *Adv. Powder Technol.* **2017**, *28*, 1882–1887. [CrossRef]
39. Mazzone, G.; Antisari, M.V. Structural and magnetic properties of metastable fcc Cu-Fe alloys. *Phys. Rev. B* **1996**, *54*, 441–446. [CrossRef]
40. Xu, J.; Collins, G.S.; Peng, L.S.J.; Atzmon, M. Deformation-assisted decomposition of unstable $Fe_{50}Cu_{50}$ solid solution during low-energy ball milling. *Acta Mater.* **1999**, *47*, 1241–1253. [CrossRef]
41. Wanderka, N.; Czubayko, U.; Naundorf, V.; Ivchenko, V.A.; Yermakov, A.Y.; Uimin, M.A.; Wollenberger, H. Characterization of nanoscaled heterogeneities in mechanically alloyed and compacted CuFe. *Ultramicroscopy* **2001**, *89*, 189–194. [CrossRef]
42. Eckert, J.; Holzer, J.C.; Krill, C.E.; Johnson, W.L. Reversible grain size changes in ball-milled nanocrystalline Fe-Cu alloys. *J. Mater. Res.* **1992**, *7*, 1980–1983. [CrossRef]
43. Hong, L.B.; Fultz, B. Two-phase coexistence in Fe-Cu alloys synthesized by ball milling. *Acta Mater.* **1998**, *46*, 2937–2946. [CrossRef]
44. Chien, C.L.; Liou, S.H.; Kofalt, D.; Yu, W.; Egami, T.; Watson, T.J.; McGuire, T.R. Magnetic properties of Fe_xCu_{100-x} solid solutions. *Phys. Rev. B* **1986**, *33*, 3247–3250. [CrossRef] [PubMed]
45. Teranishi, T.; Sato, K. OPTICAL, ELECTRICAL AND MAGNETIC PROPERTIES OF CHALCOPYRITE, $CuFeS_2$. *Le J. Phys. Colloq.* **1975**, *36*, C3-149–C3-153. [CrossRef]
46. Syafiq, U.; Ataollahi, N.; Di Maggio, R.; Scardi, P. Solution-Based Synthesis and Characterization of Cu_2ZnSnS_4 (CZTS) Thin Films. *Molecules* **2019**, *24*, 3454. [CrossRef]
47. Nautiyal, H.; Lohani, K.; Mukherjee, B.; Isotta, E.; Malagutti, M.A.; Ataollahi, N.; Pallecchi, I.; Putti, M.; Misture, S.T.; Rebuffi, L.; et al. Mechanochemical Synthesis of Sustainable Ternary and Quaternary Nanostructured Cu_2SnS_3, Cu_2ZnSnS_4, and $Cu_2ZnSnSe_4$ Chalcogenides for Thermoelectric Applications. *Nanomaterials* **2023**, *13*, 366. [CrossRef]
48. Mukherjee, B.; Isotta, E.; Fanciulli, C.; Ataollahi, N.; Scardi, P. Topological Anderson Insulator in Cation-Disordered Cu_2ZnSnS_4. *Nanomaterials* **2021**, *11*, 2595. [CrossRef]
49. Isotta, E.; Mukherjee, B.; Fanciulli, C.; Pugno, N.M.; Scardi, P. Order–Disorder Transition in Kesterite Cu_2ZnSnS_4: Thermopower Enhancement via Electronic Band Structure Modification. *J. Phys. Chem. C* **2020**, *124*, 7091–7096. [CrossRef]
50. Lohani, K.; Isotta, E.; Ataollahi, N.; Fanciulli, C.; Chiappini, A.; Scardi, P. Ultra-low thermal conductivity and improved thermoelectric performance in disordered nanostructured copper tin sulphide (Cu_2SnS_3, CTS). *J. Alloy. Compd.* **2020**, *830*, 154604. [CrossRef]
51. Nawaz, S.; Thebo, K.H.; Malik, A.Q. Deposition of $CuFeS_2$ and Cu_2FeSnS_4 thin films and nanocrystals using diisobutyldithiophosphinato-metal precursors. In Proceedings of the 2020 17th International Bhurban Conference on Applied Sciences and Technology (IBCAST), Islamabad, Pakistan, 14–18 January 2020; pp. 2–8.
52. ur Rehman, U.; Mahmood, K.; Ashfaq, A.; Ali, A.; Tahir, S.; Ikram, S.; Rehman, A.; ul Sahar, K.; Ahmad, W.; Amin, N. Enhanced thermoelectric performance of hydrothermally synthesized $CuFeS_2$ nanostructures by controlling the Cu/Fe ratio. *Mater. Chem. Phys.* **2022**, *279*, 125765. [CrossRef]

53. Wang, Y.H.A.; Bao, N.; Gupta, A. Shape-controlled synthesis of semiconducting $CuFeS_2$ nanocrystals. *Solid State Sci.* **2010**, *12*, 387–390. [CrossRef]
54. Wang, M.X.; Wang, L.S.; Yue, G.H.; Wang, X.; Yan, P.X.; Peng, D.L. Single crystal of $CuFeS_2$ nanowires synthesized through solventothermal process. *Mater. Chem. Phys.* **2009**, *115*, 147–150. [CrossRef]
55. Bastola, E.; Bhandari, K.P.; Subedi, I.; Podraza, N.J.; Ellingson, R.J. Structural, optical, and hole transport properties of earth-abundant chalcopyrite ($CuFeS_2$) nanocrystals. *MRS Commun.* **2018**, *8*, 970–978. [CrossRef]
56. Tonpe, D.; Gattu, K.; More, G.; Upadhye, D.; Mahajan, S.; Sharma, R. Synthesis of $CuFeS_2$ thin films from acidic chemical baths. *AIP Conf. Proc.* **2016**, *1728*, 020676. [CrossRef]
57. Vahidshad, Y.; Mirkazemi, S.M.; Tahir, M.N.; Ghasemzadeh, R.; Tremel, W. Synthesis of $CuFeS_2$ Nanoparticles by One-pot Facile Method. *J. Nanostruct.* **2017**, *7*, 284–291. [CrossRef]
58. Ramachandran, R.; Chen, T.W.; Veerakumar, P.; Anushya, G.; Chen, S.M.; Kannan, R.; Mariyappan, V.; Chitra, S.; Ponmurugaraj, N.; Boominathan, M. Recent development and challenges in fuel cells and water electrolyzer reactions: An overview. *RSC Adv.* **2022**, *12*, 28227–28244. [CrossRef]
59. Ding, W.; Wang, X.; Peng, H.; Hu, L. Electrochemical performance of the chalcopyrite $CuFeS_2$ as cathode for lithium ion battery. *Mater. Chem. Phys.* **2013**, *137*, 872–876. [CrossRef]
60. Senkale, S.; Indris, S.; Etter, M.; Bensch, W. $CuFeS_2$ as a Very Stable High-Capacity Anode Material for Sodium-Ion Batteries: A Multimethod Approach for Elucidation of the Complex Reaction Mechanisms during Discharge and Charge Processes. *ACS Appl. Mater. Interfaces* **2021**, *13*, 26034–26045. [CrossRef]
61. Wu, Y.; Zhou, B.; Yang, C.; Liao, S.; Zhang, W.H.; Li, C. $CuFeS_2$ colloidal nanocrystals as an efficient electrocatalyst for dye sensitized solar cells. *Chem. Commun.* **2016**, *52*, 11488–11491. [CrossRef]
62. Sathyaseelan, A.; Kesavan, D.; Manoharan, S.; Mariappan, V.K.; Krishnamoorthy, K.; Kim, S.J. Thermoelectric Driven Self-Powered Water Electrolyzer Using Nanostructured $CuFeS_2$ Plates as Bifunctional Electrocatalyst. *ACS Appl. Energy Mater.* **2021**, *4*, 7020–7029. [CrossRef]
63. Li, B.; Huang, L.; Zhong, M.; Wei, Z.; Li, J. Electrical and magnetic properties of FeS_2 and $CuFeS_2$ nanoplates. *RSC Adv.* **2015**, *5*, 91103–91107. [CrossRef]